J Mater Sci
DOI 10.1007/s10853-014-8361-6

Phase assembly and electrical conductivity of spark plasma sintered CeO_2–ZrO_2 ceramics

Rosalía Poyato · Sylvia A. Cruz · Francisco L. Cumbrera · Berta Moreno · Eva Chinarro · José A. Odriozola

Received: 30 January 2014 / Accepted: 27 May 2014

Abstract $Ce_xZr_{1-x}O_2$ ($x = 0.10$, 0.16 and 0.33) nanocrystalline powders were obtained by a two-step synthesis technique and sintered by spark plasma sintering (SPS). As consequence of the reduction of Ce^{4+} to Ce^{3+} species by carbon in the graphite environment in SPS, phase assemblies including tetragonal, monoclinic and pyrochlore phases were generated in the ceramics during the sintering process. The electrical conductivity was highly dependent on phase assembly and atmosphere (N_2, H_2 and O_2). A significant decrease in the activation energy was noticed in the ceramics with high pyrochlore content when measuring the conductivity in H_2 atmosphere, consequence of the strong reduction promoted in these ceramics during the measurement. Equal conduction behavior with similar activation energy was observed in all the ceramics when measuring in O_2 atmosphere.

Keywords CeO_2–ZrO_2 · Spark plasma sintering · Pyrochlore · Electrical conductivity

R. Poyato (✉) · S. A. Cruz · J. A. Odriozola
Instituto de Ciencia de Materiales de Sevilla, Univ. de Sevilla-CSIC, Avda. Américo Vespucio, 49, 41092 Seville, Spain
e-mail: rosalia.poyato@icmse.csic.es

F. L. Cumbrera
Dep. Física de la Materia Condensada, Univ de Sevilla, 41080 Seville, Spain

B. Moreno · E. Chinarro
Instituto de Cerámica y Vidrio, CSIC, c/Kelsen 5, 28049 Cantoblanco, Madrid, Spain

Introduction

CeO_2–ZrO_2-based materials have been widely investigated due to their great potential for different applications, such as gas sensors, solid oxide fuel cells (SOFC) or catalytic materials [1–4].

This system has been shown to be a mixed conductor unlike most stabilized zirconias. Whereas the latter are usually pure ionic conductors, the former can exhibit large electronic contributions at moderate temperatures and oxygen activities [5–8]. The defect structure of CeO_2–ZrO_2 has been described by different authors [5, 7–9] and can be summarized as follows. Due to charge neutrality considerations, a Ce^{4+} ion substituting a Zr^{4+} cannot affect any additional creation of oxygen vacancies beyond the inherent defect concentration level. However, the presence of Ce^{4+} ions on Zr^{4+} sites affects the point defect equilibria involving oxygen vacancies, as the formation of oxygen vacancies might be favored by the large size difference of the two cations ($r_i(Zr^{4+}) = 0.72$ Å; $r_i(Ce^{4+}) = 0.87$ Å, for sixfold coordination) [5, 6, 9, 10]. The second aspect is that Ce^{4+} ion is easily reduced to Ce^{3+} under suitably low oxygen partial pressures (10^{-11} to 10^{-19} atm) [11, 12]; therefore, charged oxygen vacancies are produced. These vacancies are coupled to free electrons localized on Ce^{3+} substitutional defects, giving rise to electronic conductivity through electron hopping between cerium ions [5, 7], which is strongly dependent on the ceria content [5].

The mixed conduction makes this system an interesting material for application as SOFC anode [1], and correlation between electrical and structural properties of the ceria–zirconia system has been approached in recent studies [7, 13–16]. Boaro et al. [16] have carried out a complete study of the effects of redox history on structural, chemical and electrical properties of $Ce_xZr_{1-x}O_2$ ($x = 0.20$, 0.50 and

Journal : Large 10853 | Dispatch : 5-6-2014 | Pages : 10
Article No. : 8361 | ☐ LE | ☐ TYPESET
MS Code : JMSC-D-14-00482 | ☑ CP | ☑ DISK

0.80) solid solution in order to explore the suitable operational conditions for an optimization of their use as electroactive components for SOFC anodes.

Recently, we reported on the processing and microstructural study of nanostructured 10 mol% CeO_2–ZrO_2 ceramics prepared by spark plasma sintering (SPS) [17]. This technique has emerged as a powerful tool in ceramics processing, as it allows fast densification of ceramics at relatively low temperatures and pressures by the simultaneous application of pressure and a low DC voltage to the graphite mold during heating [18–20]. We have shown that the highly reducing atmosphere created by the graphite environment during SPS promoted the gradual reduction of Ce^{4+} to Ce^{3+}, giving place to presence of pyrochlore phase when sintering at 1200 °C for 5 min. Several authors have shown that the reduction of metastable tetragonal phase, denoted as t' phase, at temperatures ≥1050 °C leads to pyrochlore phases ($Ce_2Zr_2O_{7+\delta}$) [12, 14, 21–23]; however, to the best of our knowledge, no studies have been published on the appearance of these phases in spark plasma sintered CeO_2–ZrO_2 ceramics with different CeO_2 doping concentrations and the effect of phase formation on the conductivity in this system.

In this study, 10, 16 and 33 mol% CeO_2-doped ZrO_2 powders were obtained by means of a two-step synthesis route and subsequently sintered by SPS. Phase assembly of the ceramics was analyzed by X-ray diffraction and Rietveld refinement. The effect of the CeO_2 content on the phase assembly of the ceramics was investigated. The electrical conductivity as a function of temperature (200–900 °C) was analyzed in three different atmospheres. The structural characterization was of prime relevance for understanding the electrical conductivity results as the different conduction mechanisms found were related to the phase assembly of the ceramics.

Experimental procedure

Powder synthesis and characterization

According to the phase diagram for the system Ce_2O_3–ZrO_2 [24], the compound $Ce_2Zr_2O_7$ with pyrochlore structure is in equilibrium with monoclinic/tetragonal phases above and below 1000 °C, respectively, for compositions with Zr/Ce atomic ratios between 1.3 (44 mol% Ce_2O_3) and 32.3 (3 mol% Ce_2O_3). Thus, the formation of the pyrochlore cubic structure stabilizes the ZrO_2 tetragonal phase, promoting an increase of ionic conductivity by increase of the oxygen vacancies, as a consequence of the substitution of Ce^{3+} for Zr^{4+}. Using this phase diagram, the CeO_2 compositions (10, 16 and 33 mol% CeO_2) were selected among those that stabilize the tetragonal phase by the formation of pyrochlore phase.

$Ce_{0.10}Zr_{0.90}O_2$ (CeZr10), $Ce_{0.16}Zr_{0.84}O_2$ (CeZr16) and $Ce_{0.33}Zr_{0.67}O_2$ (CeZr33) mixed oxides were synthesized by a two-step synthesis procedure. In a first step, a hydrothermal route was followed to synthesize nanocrystalline ZrO_2 powder. Zirconyl nitrate hydrate ($ZrO(NO_3)\cdot xH_2O$, 0.5 M, <90 % purity) and sodium hydroxide (NaOH, 5 M) were mixed together and sonicated for 30 min. Later, 10 mL of the solution was disposed in the hydrothermal vessel with 2 mL of ethanol, closed and heated in a furnace for 5 h at 200 °C. When the vessel achieved room temperature, the solid was washed with distilled water and dried at 100 °C for 1 h. In a second step, cerium oxide was deposited onto the ZrO_2 particles by the impregnation method. The adequate amount of 1 M $Ce(NO)_3\cdot 6H_2O$ solution (99.5 % purity) was added to the solid in order to obtain 10, 16 or 33 mol% CeO_2–ZrO_2 powders. The resulting slurries were then dried for 12 h at 100 °C. Finally, the ceramic powders were calcined at 700 °C for 4 h. The powders were suspended in aqueous solution and subjected to ultrasonic agitation in order to reduce agglomeration before their analysis.

X-ray diffraction (PANalytical X'Pert Pro diffractometer) was used for phase identification of the powders. Diffraction patterns were recorded using Cu Kα radiation over a 2θ range of 10°–90° and a position-sensitive detector using a step size of 0.05°2θ and a counting time of 1 s per step.

The cerium and zirconium contents of the samples were determined by X-ray fluorescence spectrometry (XRF-Panalytical AXIOS PW4400) sequential spectrophotometer with a rhodium tube as the source of radiation.

Ceramics processing and characterization

SPS (Model 515S, SPS Dr Sinter Inc., Kanagawa, Japan) of the ceramic powders was performed in a vacuum in a 15-mm-diameter cylindrical graphite die/punch setup, under a uniaxial pressure of 50 MPa at 1200 °C for 5 min or without holding time. The heating rate was 100 °C/min. The applied pressure was maintained throughout the entire thermal cycle. Hereinafter, we will refer to the sintered samples as CeZr10-0 min, CeZr10-5 min, CeZr16-0 min and CeZr33-0 min. Temperature was measured by using a thermocouple, which was placed in a bore hole in the middle part of the graphite die. The sintered ceramics of approximately 15 mm × 2 mm were polished in order to eliminate the surface carbon. Density of the ceramics was determined using the Archimedes method, using water as the immersion liquid. Theoretical density for each composition was calculated according to:

Journal : Large 10853 | Dispatch : 5-6-2014 | Pages : 10
Article No. : 8361 | ☐ LE | ☐ TYPESET
MS Code : JMSC-D-14-00482 | ☑ CP | ☑ DISK

$$\text{Theoretical density} = (\text{density } (CeO_2)) * \text{wt}\%(CeO_2) + (\text{density } (ZrO_2)) * \text{wt}\%(ZrO_2).$$

In order to approach phase identification and structural characterization, powder diffraction patterns were collected on the polished, cross-section surfaces of the ceramics. The step scan technique was used with a step size of 0.02°2θ and a counting time of 10 s at each point.

Rietveld refinements were performed using the FULLPROF software [25]. In this method, a least-squares refinement of a crystallographic model is performed until a satisfactory fit is achieved between the theoretical diffractogram and the experimental data. A pseudo-Voigt function was chosen to describe the peak shape, and the refinement included the following parameters: (1) the background, generated by linear interpolation of a set of background points with refinable heights; (2) the scale factors; (3) the global instrumental parameters (zero-point 2θ shift and systematic shifts, depending on transparency and off-centering of the sample); (4) the lattice parameters for all phases; (5) the profile parameters (Caglioti half-width parameters and the mixing parameter, η, of the pseudo-Voigt function) [26]; (6) refinable atom coordinates; and (7) occupancy factors for all atomic species.

Quantitative phase analysis with the Rietveld method relies on the simple relationship:

$$W_i = S_i(ZMV)/\sum_{i=1}^{n} S_j(ZMV)_j$$

where W_i is the relative weight fraction of the phase i in a mixture of n phases, and S, Z, M and V are, respectively, the Rietveld scale factor, the number of formula units per cell, the mass of the formula unit and the unit cell volume. Among the profile parameters, it can be outlined the full width at half maximum (FWHM), which is usually expressed as a quadratic form in tanθ, as introduced by Caglioti et al. [27]:

$$(\text{FWHM})^2 = U\tan^2\theta + V\tan\theta + W$$

depending on the U, V and W refinable parameters.

Taking into account that many materials have non-stoichiometry deviations and different kinds of disorder, the refinement of site occupancy is required. The site occupancy factors (f) can be defined as the fraction of atoms in a particular Wyckoff position in such a way that $f = 1$ indicates full occupancy.

The quality of the Rietveld refinement is quantified by several figures of merit [28]: profile residual, R_p, weighted profile residual, R_{wp}, expected residual, R_{exp}, and Bragg residual R_B. In any case, none of these residuals is a substitute for the plots of the observed and calculated patterns, supplemented by the differences plotted on the same scale.

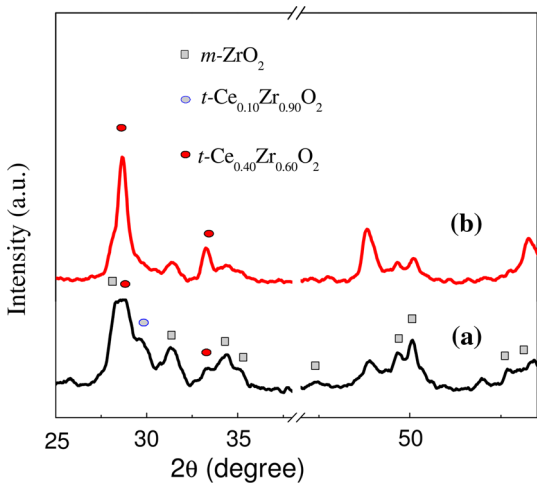

Fig. 1 XRD patterns of the calcined CeO_2–ZrO_2 powders with 16 mol% CeO_2 (*a*) and 33 mol% CeO_2 (*b*)

Microstructural investigation was performed by scanning electron microscopy (Hitachi S4800 SEM-FEG).

Electrical properties were measured by impedance spectroscopy with an Agilent 4294A equipment; two-point measurements were performed on the samples sandwiched between Pt foils that acted as electrodes and that contacted the sample through simple mechanical pressure. Pt paste electrodes were not applied to the samples before testing, since microstructural changes could be induced during electrode firing. The samples were placed in a tubular furnace where atmosphere and temperature were controlled. Measurements were acquired in N_2, H_2 and O_2 atmosphere, and oxygen partial pressure was not recorded while measuring, in the frequency range from 40 to 10^7 Hz and varying the temperature from 200 to 900 °C. The conductivity values were determined after fitting the spectra with the Zview software.

Results and discussion

The XRD patterns for the calcined CeZr16 and CeZr33 powders are presented in Fig. 1. It has been published [17] that the presence of monoclinic ZrO_2 phase (JCPDS 01-078-0047) in the starting powder is clear. However, when increasing the CeO_2 content to 10 mol%, other phases are found [17]. In the powders with 16 mol% CeO_2, the tetragonal solid solution (JCPDS 01-080-0) is present, and the $Ce_{0.40}Zr_{0.40}O_2$ solid solution is found in the powders with 16 and 33 mol% CeO_2. Also, a decrease in the peaks corresponding to the monoclinic ZrO_2 phase is observed in the two powders with higher CeO_2 content. The observed phases are in agreement with the phase

Journal : Large 10853 Dispatch : 5-6-2014 Pages : 10
Article No. : 8361 LE TYPESET
MS Code : JMSC-D-14-00482 CP DISK

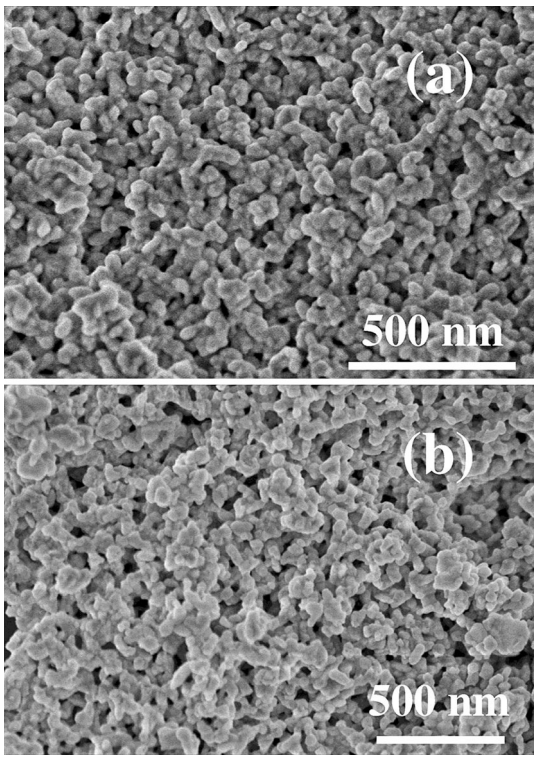

Fig. 2 SEM micrographs of **a** the calcined 16 mol% CeO_2–ZrO_2 powder and **b** the calcined 33 mol% CeO_2–ZrO_2 powder

Table 1 Density, relative density and grain size of the ceramics

Ceramic	Theoretical density (g/cm^3)	Measured density (g/cm^3)	Relative density (%)	Grain size (nm)	
				Core region	Edge region
CeZr16-0 min	5.97	5.85	98.0	50–70	50–70
CeZr33-0 min	6.13	5.60	91.4	40–70	100–150

diagram reported by Kaspar et al. [29] for CeO_2–ZrO_2 solid solution. The same crystallite size (20 nm) was obtained for all compositions.

The cerium and zirconium contents of the powders, determined by XRF, are identical as the nominal ones. SEM micrographs of the calcined CeZr16 and CeZr33 powders show a spherical shape and a grain size lower than 100 nm in both of them (Fig. 2). Similar characteristics have been published for the calcined CeZr10 powder [17].

Table 1 shows density and relative density of the sintered ceramics. Nearly full densification (>98 % TD) was obtained in the CeZr16-0 min ceramic, similar to the reported result for the CeZr10-0 min and CeZr10-5 min ceramics [17], whereas a lower relative density, 91.4 %, was measured in the ceramic with higher CeO_2 content. No micro- or macrocracks were observed in the ceramics, conversely to the results published by Huang et al. [30] for similar materials. These authors reported the existence of macrocracks in 12 mol% CeO_2-doped ZrO_2 ceramics prepared by SPS and related this fact to the presence of a large amount of monoclinic ZrO_2 phase.

Using the experimental X-ray diffraction patterns, Rietveld refinements were carried out in CeZr16-0 min and CeZr33-0 min ceramics. In a first analysis of the CeZr16-0 min ceramic, four phases were discerned, tetragonal, monoclinic, cubic pyrochlore and some residual graphite, this latter most likely being a rest of the graphite foil used during SPS that was not suitably removed. In an earlier study [17], we have shown that the highly reducing atmosphere created by the graphite environment during SPS promotes the reduction of Ce^{4+} to Ce^{3+} in CeO_2–ZrO_2 ceramics, and the obtained phases are in agreement with the ZrO_2–Ce_2O_3 phase diagram [24].

However, during the analysis of the Rietveld refinement of the CeZr16-0 min ceramic, we noted that the pyrochlore amount [54.1(7) wt%] was quite high given the Ce available in the system (16 mol%). Moreover, when refining the occupancy factors, it was found that almost all the Ce is present in the pyrochlore phase, and a composition of $Zr_{3.26}Ce_{0.74}O_{7.63}$ was obtained, which implies that in this phase Ce and Zr are not in 1:1 stoichiometry. Besides that, the reliability factors (i.e., $\chi^2 = 5.60$) are not fully satisfactory, a fact that is particularly true for the R_B and R_F residuals associated with the cubic pyrochlore phase. This disagreement, together with the anomalous stoichiometry of this phase, far from the usual formula $A_2B_2O_7$ of the pyrochlore oxides, led us to evaluate an alternative model for the pyrochlore structure.

In fact, other authors have reported for some particular pyrochlore systems alternative groups of symmetry to the usual cubic $Fd\bar{3}m$. Taking into account the maximal subgroups of the $Fd\bar{3}m$, Thomson et al. [31] proposed the rhombohedral $R\bar{3}m$ group of symmetry for $Ce_2Zr_2O_{7.97}$, whereas Sasaki et al. [32] found the cubic phase $F\bar{4}3m$ for the composition $Ce_2Zr_2O_{7.5}$. Kishimoto et al. [33] found the $P2_13$ group of symmetry for the $Ce_2Zr_2O_8$ composition (also called κ-$CeZrO_4$ phase), although this last group is not a subgroup of the original $Fd\bar{3}m$. In a first stage, we tested these structures for our pyrochlore phase, but the Rietveld refinement worsened in relation to our first conventional refinement. In the same way, we have investigated, with negative results, the possibility of the δ-phase, reported by Thornber et al. [34]: a fluorite-related structure with different stoichiometries for both kinds of cations.

By considering that according to Wuensch et al. [35], pyrochlore is the only oxide in which simultaneous order–disorder transformations take place for both the anion and cation arrays in structure, we proposed a new model with

Journal : Large 10853 Dispatch : 5-6-2014 Pages : 10
Article No. : 8361 LE TYPESET
MS Code : JMSC-D-14-00482 CP DISK

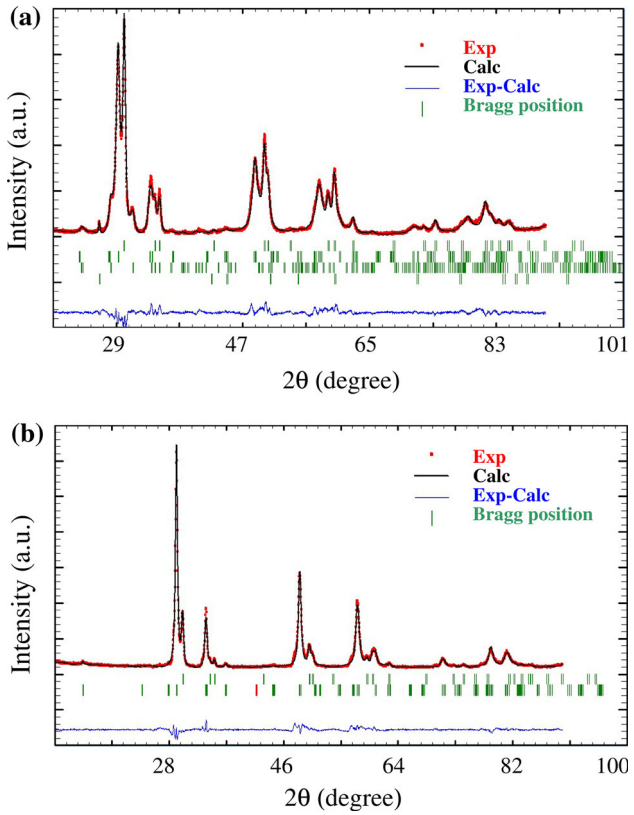

Fig. 3 Rietveld refined powder XRD data for **a** the CeZr16-0 min ceramic and **b** the CeZr33-0 min ceramic

Table 2 Rietveld refinement of the CeZr16-0 min ceramic

Phase	Tetragonal pyrochlore	Tetragonal	Monoclinic	Graphite
Fraction (wt%)	50.0 (4)	31.6 (2)	13.4 (4)	4.9 (2)
a (Å)	7.489 (8)	3.6051 (7)	5.276 (3)	2.413 (3)
b (Å)	7.489 (8)	3.6051 (7)	5.259 (3)	2.413 (3)
c (Å)	10.477 (1)	5.197 (1)	5.165 (3)	6.707 (2)
β	–	–	98.69 (3)	–
Group of symmetry	$I4_1/amd$	$P4_2/nmc$	$P2_1/c$	$P6_3/mmc$
R_{wp}	4.78			
R_{exp}	2.18			
χ^2	4.83			

Table 3 Reliability parameters of the cubic and tetragonal models for the pyrochlore structure

	Cubic pyrochlore	Tetragonal pyrochlore
R_{wp}	5.60	4.78
R_{exp}	2.18	2.18
χ^2	6.6	4.83
R_B	3.7	1.50
R_F	1.97	1.01

Table 4 Rietveld refinement of the CeZr33-0 min ceramic

Phase	Tetragonal Pyrochlore	Tetragonal
Fraction (wt%)	81.61 (9)	18.4 (6)
$a = b$ (Å)	7.5115 (9)	3.6100 (6)
c (Å)	10.574 (2)	5.202 (1)
Group of symmetry	$I4_1/amd$	$P4_2/nmc$
R_{wp}	7.32	
R_{exp}	3.67	
χ^2	3.99	

the tetragonal I41/amd symmetry. In fact, this is the only maximal subgroup of the $Fd\bar{3}m$ group in the tetragonal system. Transformations of order for cation, anion or both arrays could justify this reduction in symmetry. For this new Rietveld refinement, cation occupancies were freely refined in both 8c and 8d sites, with the only constraint of full occupancy at each site. This can be justified as long as the XRD pattern is largely dominated by the scattering of the heavy cations. For this reason, the same accuracy is not possible for oxygen atoms, for which we allowed the possibility of partial occupancy and vacancies in 16g, 8e, 4a and 4b sites but maintained the constraint of global charge balance. The starting lattice parameters were obtained with the indexing software TREOR [36] applied to the first 20 observed pyrochlore reflections. A promising de Wolff [37] figure of merit M(20) = 88 was obtained.

Plot of the Rietveld refinement corresponding to the CeZr16-0 min sintered ceramic is given in Fig. 3a. The main results of the Rietveld analysis are shown in Table 2. The major crystalline phase is the Ce-deficient tetragonal pyrochlore [50.0(4) wt%], with an axial ratio $c/a\sqrt{2} = 0.989$, highlighting the pseudocubic character of that tetragonal phase of composition $Zr_{3.21}Ce_{0.78}O_{7.59}$. Contributions of tetragonal [31.6(2) wt%] and monoclinic [13.4(4) wt%] phases and a trace of residual graphite [4.9(2) wt%] were also present in the refinement.

In Table 3, we report the comparison between the reliability parameters for both models, cubic and tetragonal. The reported results support the superiority of our tetragonal model. To the best of our knowledge, this is the first time that a tetragonal pyrochlore has been reported in the literature for this system. Additional crystallographic data for this new structure will be reported elsewhere.

The Rietveld analysis for the CeZr33-0 min ceramic was also modeled taking into account the tetragonal variant of the pyrochlore structure just introduced, and the

Journal : Large 10853 Dispatch : 5-6-2014 Pages : 10
Article No. : 8361 LE TYPESET
MS Code : JMSC-D-14-00482 CP DISK

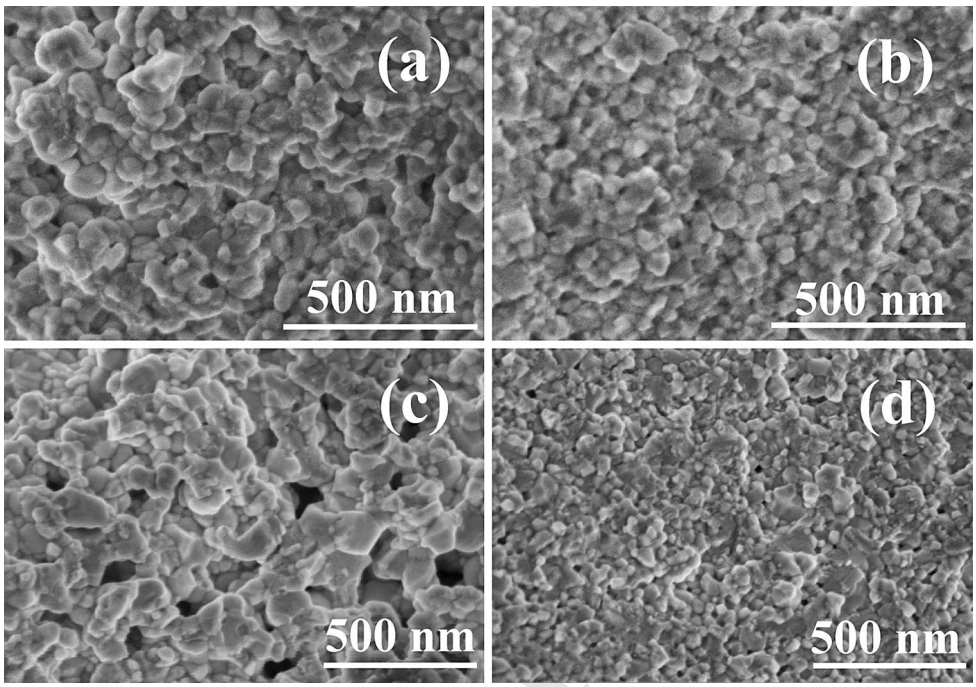

Fig. 4 SEM micrographs of the surface (**a**) and core (**b**) area of the CeZr16-0 min ceramic and the surface (**c**) and core (**d**) area of the CeZr33-0 min ceramic

refinement indicated the formation of only two phases (Table 4). The major crystalline phase is the Ce-deficient tetragonal pyrochlore structure [81.6(9) wt%] and the minor phase the tetragonal one [18.4(6) wt%]. Plot of the Rietveld refinement corresponding to the CeZr33-0 min sintered ceramic is given in Fig. 3b. In this case, the refinement of the occupancy factors led to a composition $Zr_{2.8}Ce_{1.2}O_{7.4}$ for the pyrochlore structure, and an axial ratio $c/a\sqrt{2} = 0.995$, also pseudocubic but more distorted as compared to the previous ceramic.

The described phase assemblies are quite different than the reported ones for the 10 mol% CeO_2–ZrO_2 ceramics sintered for 5 min and without holding time [17]. In these cases, whereas in the latter the major crystalline phase is metastable tetragonal, t' (90.9 wt%), and the minor phase is tetragonal (9.1 wt%), in the former the phases were tetragonal (82.5 wt%), monoclinic (15.1 wt%) and pyrochlore (2.4 wt%). We showed [17] that the obtained phases are consequence of the highly reducing atmosphere created by the graphite environment during SPS, which promotes the reduction of Ce^{4+} ions to Ce^{3+}. However, the pyrochlore phase was found only when the sintering temperature was held for 5 min. On the contrary, when the CeO_2 amount increases to 16 and 33 mol%, even when sintering without holding time the tetragonal phase is destabilized and great amounts of pyrochlore phase are present in both ceramics. Also, we have found that the cubic pyrochlore phase declined into tetragonal pyrochlore. The reduction of Ce^{4+} ions to Ce^{3+} in the CeZr33-0 min ceramic promotes also the presence of some porosity in this ceramic (Table 1), as a consequence of oxygen loss.

The SEM micrographs of the CeZr16-0 min and CeZr33-0 min ceramics are shown in Fig. 4. Fracture surface was analyzed in order to avoid possible oxidation during polishing and etching. A homogeneous microstructure with a grain size about 50–70 nm in the whole ceramic is observed in the CeZr16-0 min ceramic. This microstructure is similar to the reported one for the CeZr10-0 min ceramic [17]. Conversely, a graded microstructure with 100–150 nm grain size in the edge region and 40–70 nm grain size in the core region is observed in the CeZr33-0 min ceramic (Table 1). Graded microstructures have been previously reported for samples similar to the ones under study [27]. During SPS, the edge has much lower oxygen partial pressure, which could lead to a gradient of Ce^{4+} reduction to Ce^{3+} from outside to inside. Whereas for the CeZr16-0 min ceramic it is thought that most of the Ce^{4+} has converted to Ce^{3+} according to the homogeneous microstructure, for the CeZr33-0 min it looks like the reduction beneath the edge area was not as fast and complete as that of the edge area, giving rise to the graded microstructure.

Nyquist plots measured on the CeZr10-0 min and CeZr33-0 min ceramics at 600 °C are shown in Fig. 5. These compositions have been selected on the basis of their Ce content. The spectra obtained have been fitted to an equivalent circuit composed by two RQs (constant phase element in parallel with a resistance) connected in series

Journal : Large 10853 Dispatch : 5-6-2014 Pages : 10
Article No. : 8361 LE TYPESET
MS Code : JMSC-D-14-00482 CP DISK

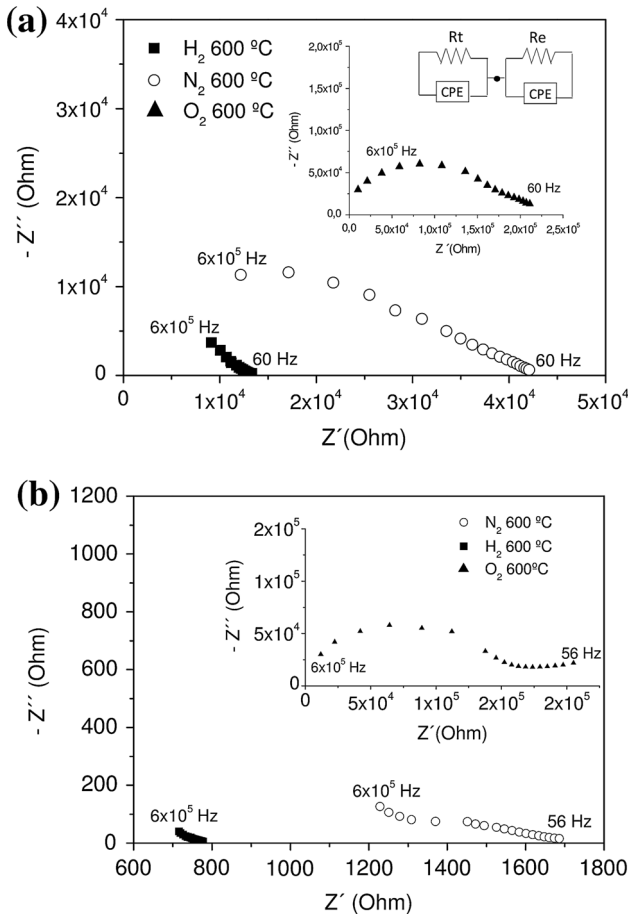

Fig. 5 Nyquist plots of the **a** CeZr10-0 min and **b** CeZr33-0 min ceramics, measured in N_2, H_2 and O_2 atmospheres at 600 °C

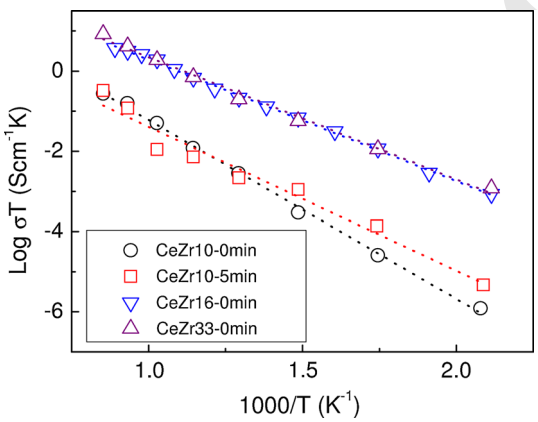

Fig. 6 Electrical conductivity versus temperature measured in the sintered ceramics in nitrogen atmosphere

(inset in Fig. 5a). The first one has been ascribed to the material, while the second one is related to the interface between the electrode and the ceramic sample. On this sense, the conductivity has been calculated from intercept

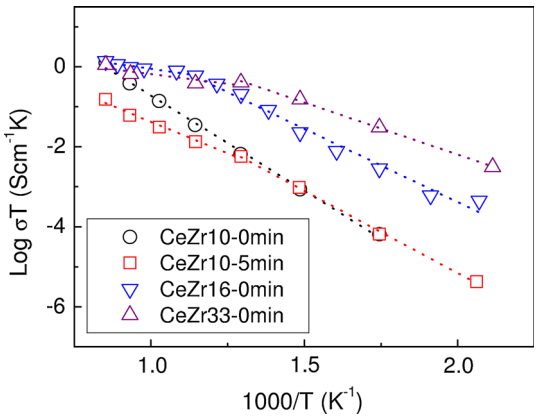

Fig. 7 Electrical conductivity versus temperature measured in the sintered ceramics in hydrogen atmosphere

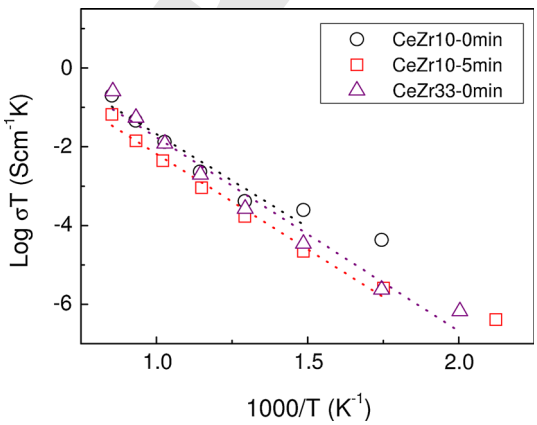

Fig. 8 Electrical conductivity versus temperature measured in the sintered ceramics in oxygen atmosphere

of the first semicircle with the real part of impedance. This value represents the total conductivity of the material, while the arc corresponding to the ceramic–electrode interface was not analyzed in this work.

Figures 6, 7 and 8 show the Arrhenius plots for all the studied ceramics measured in N_2, H_2 and O_2 atmosphere, respectively. The slope of these diagrams has been used to calculate the activation energy of the conducting species (Table 5).

It is clear that the Arrhenius plots are highly dependent on the ceramic phase assembly. In the CeZr10-0 min ceramic (metastable t' phase: 91 wt%, tetragonal phase: 9 wt% [17]), single activation energies were evidenced for the whole temperature range in the three different atmospheres, pointing out to the existence of only one conduction mechanism. A value close to 0.85 eV was obtained in the three cases, very similar to the reported one by previous authors [5, 6, 8] for ceramics with similar

Journal : Large 10853 Dispatch : 5-6-2014 Pages : 10
Article No. : 8361 LE TYPESET
MS Code : JMSC-D-14-00482 CP DISK

Table 5 Phase assembly and electrical properties of the sintered ceramics

Ceramic	Phases from Rietveld refinement (wt%)	E_a (eV)			
		N_2 atmosphere	H_2 atmosphere		O_2 atmosphere
			200–500 °C	500–900 °C	
CeZr10-0 min	t' 90.9 %, t 9.1 %	0.85	0.90		0.90
CeZr10-5 min	t 82.5 %, m 15.1 %, p 2.4 %	0.68	0.78	0.60	0.92
CeZr16-0 min	t 31.6 %, m 13.4 %, p 50.0 %	0.58	0.70	0.20	–
CeZr33-0 min	t 18.4 %, p 81.6 %	0.58	0.49	0.18	0.93

composition and phases, and equilibrium defect concentrations. This result is consistent with the activation energy for oxygen vacancy conduction in zirconia-based ceramic oxides [5, 6], where the electronic contribution to the total conductivity is not significant comparing with the ionic. The lower value of conductivity was registered when measuring in the O_2 atmosphere. This is consequence of the re-oxidation of the Ce^{3+} ions to Ce^{4+}, which eliminates the electronic conductivity of the samples.

In the CeZr10-5 min, CeZr16-0 min and CeZr33-0 min ceramics, with more complex phase assemblies, different behavior was obtained as a function of the present phases and also as a function of the measuring atmosphere. Differences were observed in the activation energies as a function of the amount of pyrochlore phase in these ceramics, when the conductivity was measured in N_2 (Table 5). In the two ceramics showing a high amount of pyrochlore, activation energy of 0.58 eV was obtained. This value is very similar to the reported one by Baidya et al. [14] for the $Ce_2Zr_2O_7$ phase, which is shown to be an n-type semiconductor in the temperature range 400–850 K. Thus, we can conclude that the pyrochlore phase is controlling the conducting behavior in these two ceramics. In the CeZr10-5 min ceramic, with only a 2.40 wt% pyrochlore phase, an activation energy of 0.68 eV was found, which is an intermediate value between the corresponding one for oxygen vacancy conduction (0.85 eV) and the corresponding one for n-type conduction (0.5 eV). In this ceramic, the low percentage of pyrochlore can significantly modify the conducting behavior of the material.

It is noticeable that whereas the Arrhenius plots obtained in N_2 and O_2 were straight lines, a slope change was noticed around 500 °C when measuring the conductivity in H_2 atmosphere. In the CeZr10-5 min ceramic, the activation energy decreases from 0.78 to 0.60 eV. In the CeZr16-0 min and CeZr33-0 min ceramics, the observed decrease in activation energy is more significant, with values of 0.18–0.20 eV in the high temperature range (500–900 °C).

The changes in the Arrhenius plots slope have been usually related to changes in physical or chemical structure or to the existence of two conduction mechanisms [5, 6]. Temperature programmed reduction (TPR) studies carried out by different authors in the CeO_2–ZrO_2 system [14, 23] have shown the existence of two peaks around 450–550 and 700–800 °C on the hydrogen uptake for $Ce_xZr_{1-x}O_2$ reduction. The oxygen stoichiometries estimated from the quantity of hydrogen uptake showed that the first step reduction corresponds to $Ce_2Zr_2O_7$ (pyrochlore I) and the second step reduction corresponds to $Ce_2Zr_2O_{6.2}$ (pyrochlore II) [14].

Taking these reports into account, the decrease in slope in the high temperature range described above may be clarified. In the ceramic with initially only 2.40 wt% pyrochlore phase, a higher degree of reduction could be achieved during the conductivity measurement in H_2 atmosphere, which resulted in a structural change into a higher amount of pyrochlore. Thus, an activation energy corresponding to n-type conduction was obtained in this ceramic. In the CeZr16-0 min and CeZr33-0 min ceramics, the pyrochlore amounts were initially 50.0 and 81.6 wt%, respectively. Thus, during the conductivity measurement in the highly reducing atmosphere, the pyrochlore I could be strongly reduced into $Ce_2Zr_2O_{6.2}$. This phase has been shown to have a significantly low resistivity, which remains constant in the 400–1000 K range [14]. Activation energy of 0.08 eV was reported for lower temperatures. Thus, the low activation energies found in the CeZr16-0 min and CeZr33-0 min ceramics are clearly related to the presence of $Ce_2Zr_2O_{6.2}$ phase.

Regarding the conductivity values, higher values were obtained in the CeZr16-0 min and CeZr33-0 min ceramics in the whole range of temperature, when measuring in N_2 and H_2 atmosphere. This is clearly related to the presence of pyrochlore in the ceramics.

When characterizing the ceramics in O_2 atmosphere, very similar Arrhenius plots were found in all of them. Activation energy $\sim$0.9 eV was found in all the ceramics; thus, the electrical conductivity shows the typical ionic conduction behavior, and the oxygen anti-Frenkel defects are the predominant defects. It is clear that the re-oxidation of the ceramics promoted a decrease in the concentration of oxygen vacancies, as the lower conductivity values were obtained when measuring in O_2 atmosphere.

Journal : Large 10853 Dispatch : 5-6-2014 Pages : 10
Article No. : 8361 LE TYPESET
MS Code : JMSC-D-14-00482 CP DISK

Conclusions

Spark plasma sintering of $Ce_xZr_{1-x}O_2$ ($x = 0.10$, 0.16 and 0.33) powders obtained by a two-step synthesis technique resulted in ceramics with different phase assemblies, as a consequence of the reduction of Ce^{4+} to Ce^3 in the highly reducing atmosphere created by the graphite environment during the sintering process. Phase identification carried out by means of Rietveld refinements showed the presence of a Ce-deficient tetragonal pyrochlore as the major phase in the ceramics with higher CeO_2 content, with tetragonal and monoclinic as minor phases.

The electrical conductivity of the ceramics was highly dependent on the phase assembly, and higher conductivity values were obtained in the ceramics with higher pyrochlore content, when measuring in N_2 and H_2 atmosphere. Whereas the ceramics with tetragonal phase showed an ionic conduction by oxygen vacancies independent of the atmosphere, a significant effect of the measuring atmosphere was observed in the ceramics with pyrochlore phase. A n-type semiconducting behavior seems to manage the conduction mechanism in the latter when measuring in N_2. However, a significant decrease in the activation energy was noticed around 500 °C when measuring the conductivity in H_2 atmosphere, consequence of the strong reduction promoted in these ceramics during the measurement. However, similar activation energies were observed for all compositions measured in O_2, which corresponds to ionic conduction behavior reported in the literature.

Acknowledgements Dr. Cruz thanks Junta de Andalucía (TEP-1048) for her fellowship. The financial support for this work has been obtained from the Spanish Ministerio de Ciencia e Innovación (ENE2009-14522-C05-01) and (ENE2009-14522-C05-03). Cofinanced by FEDER funds from the European Union and from Junta de Andalucía (P09-TEP-5454).

References

1. Kaspar J, Fornasiero P, Graziani M (1999) Use of CeO_2-based oxides in the three-way catalysis. Catal Today 50(2):285–298
2. Trovarelli A (2002) Catalysis by ceria and related materials. Imperial College press, London
3. Fergus JW (2006) Oxide anode materials for solid oxide fuel cells. Solid State Ion 177(17–18):1529–1541
4. Boaro M, Vicario M, Llorca J, de Leitenburg C, Dolcetti G, Trovarelli A (2009) A comparative study of water gas shift reaction over gold and platinum supported on ZrO_2 and CeO_2–ZrO_2. Appl Catal B Environ 88(3–4):272–282
5. Reidy RF, Simkovich G (1993) Electrical conductivity and point defect behavior in ceria-stabilized zirconia. Solid State Ion 62(1–2):85–97
6. Chiodelli G, Flor G, Scagliotti M (1996) Electrical properties of the ZrO_2–CeO_2 system. Solid State Ion 91(1–2):109–121
7. Boaro M, Trovarelli A, Hwang JH, Mason TO (2002) Electrical and oxygen storage/release properties of nanocrystalline ceria–zirconia solid solutions. Solid State Ion 147(1–2):85–95
8. Lee JH, Yoon SM, Kim BK, Lee HW, Song HS (2002) Electrical conductivity and defect structure of CeO_2–ZrO_2 mixed oxide. J Mater Sci 37(6):1165–1171
9. Lee JH, Yoon SM, Kim BK, Kim J, Lee HW, Song HS (2001) Electrical conductivity and defect structure of yttria-doped ceria-stabilized zirconia. Solid State Ion 144(1–2):175–184
10. Shannon RD (1976) Revised effective ionic radii and systematic studies of interatomic distances in halides and chalcogenides. Acta Cryst A 32:751–767
11. Otake T, Yugami H, Naito H, Kawamura K, Kawada T, Mizusaki J (2000) Ce^{3+} concentration in ZrO_2–CeO_2–Y_2O_3 system studied by electronic Raman scattering. Solid State Ion 135(1–4):663–667
12. Huang S, Li L, Van der Biest O, Vleugels J (2005) Influence of the oxygen partial pressure on the reduction of CeO_2 and CeO_2–ZrO_2 ceramics. Solid State Sci 7(5):539–544
13. Belous AG, Kravchyk KV, Pashkova EV, Bohnke O, Galven C (2007) Influence of the chemical composition on structural properties and electrical conductivity of Y–Ce–ZrO_2. Chem Mater 19(21):5179–5184
14. Baidya T, Hegde MS, Gopalakrishnan J (2007) Oxygen-release/storage properties of $Ce_{0.5}M_{0.5}O_2$ (M=Zr, Hf) oxides: interplay of crystal chemistry and electronic structure. J Phys Chem B 111(19):5149–5154
15. Song SD, Fuentes RO, Baker RT (2010) Nanoparticulate ceria–zirconia anode materials for intermediate temperature solid oxide fuel cells using hydrocarbon fuels. J Mater Chem 20(43):9760–9769
16. Boaro M, Desinan S, Abate C, Ferluga M, de Leitenburg C, Trovarelli A (2001) Study on redox, structural and electrical properties of $Ce_xZr_{1-x}O_2$ for applications in SOFC anodes. J Electrochem Soc 158(2):22–29
17. Cruz SA, Poyato R, Cumbrera FL, Odriozola JA (2012) Nanostructured spark plasma sintered Ce-TZP ceramics. J Am Ceram Soc 95(3):901–906
18. Omori M (2000) Sintering, consolidation, reaction and crystal growth by the spark plasma system (SPS). Mat Sci Eng A 287:183–188
19. Munir ZA, Anselmi-Tamburini U, Ohyanagi M (2006) The effect of electric field and pressure on the synthesis and consolidation of materials: a review of the spark plasma sintering method. J Mater Sci 41(3):763–777
20. Anselmi-Tamburini U, Garay JE, Munir ZA (2006) Fast low-temperature consolidation of bulk nanometric ceramic materials. Scr Mater 54(5):823–828
21. Omata T, Kishimoto H, Otsuka-Yao-Matsuo S, Ohtori N, Umesaki N (1999) Vibrational spectroscopic and X-ray diffraction studies of cerium zirconium oxides with Ce/Zr composition ratio = 1 prepared by reduction and successive oxidation of t'-$(Ce_{0.5}Zr_{0.5})O_2$ phase. J Solid State Chem 147(2):573–583
22. Hui Z, Nicolas G, Francoise V, Michele P (2003) Preparation and electrical properties of a pyrochlore-related $Ce_2Zr_2O_{8-x}$ phase. Solid State Ion 160(3–4):317–326
23. Ouyang J, Yang HM (2009) Investigation of the oxygen exchange property and oxygen storage capacity of $Ce_xZr_{1-x}O_2$ nanocrystals. J Phys Chem C 113(17):6921–6928
24. Leonov AI, Andreeva AB, Keler EK (1966) Influence of the gas atmosphere on the reaction of zirconium dioxide with oxides of cerium. Izq Akad Nauk SSSR Neorganicheskie Mater 2:137–144
25. Rodriguez-Carvajal J (1990) FULLPROF: a program for Rietveld refinement and pattern matching analysis. In: Abstracts of the satellite meeting on powder diffraction of the XV congress of the IUCr, pp 127–130
26. Ortiz AL, Sánchez-Bajo F, Padture NP, Cumbrera FL, Guiberteau F (2001) Quantitative polytype-composition analyses of SiC using

Journal : Large 10853 | Dispatch : 5-6-2014 | Pages : 10
Article No. : 8361 | LE | TYPESET
MS Code : JMSC-D-14-00482 | CP | DISK

X-ray diffraction: a critical comparison between the polymorphic and the Rietveld methods. J Eur Ceram Soc 21:1237–1248
27. Caglioti G, Paoletti A, Ricci FP (1958) Choice of collimators for a crystal spectrometer for neutron diffraction. Nucl Inst 3:223–228
28. Pecharsky VK, Zavalij PY (2009) Fundamentals of powder diffraction and structural characterization of materials, 2nd edn. Springer, Berlin
29. Kaspar J, Formagiero P (2002) Structural properties and thermal stability of ceria-zirconia and related materials. In: Trovarelli A (ed) Catalysis by ceria and related materials. Imperial College press, London, pp 217–241
30. Huang SG, Van der Biest O, Vleugels J, Vanmeensel K, Li L (2007) Characterization of Y_2O_3, CeO_2 and Y_2O_2 + CeO_2FGM tetragonal ZrO_2 ceramics by spark plasma sintering. Key Eng Mater 333:231–234
31. Thomson JB, Armstrong AR, Bruce PG (1999) An oxygen-rich pyrochlore with fluorite composition. J Solid State Chem 148:56–62
32. Sasaki T, Ukyo Y, Kuroda K, Arai S, Muto S, Saka H (2004) Crystal structure of $Ce_2Zr_2O_7$ and β-$Ce_2Zr_2O_{7.5}$. J Ceram Soc Jpn 112:440–444
33. Kishimoto H, Omata T, Otsuka-Yao-Matsuo S, Ueda K, Hosono H, Kawazoe H (2000) Crystal structure of metastable κ-$CeZrO_4$ phase possessing an ordered arrangement of Ce and Zr ions. J Alloys Compd 312:94–103
34. Thornber MR, Bevan DJM, Graham J (1968) Mixed oxides of the type MO_2(fluorite)–M_2O_3. III. Crystal structures of the intermediate phases $Zr_5Sc_2O_{13}$ and $Zr_3Sc_4O_{12}$. Act Cryst B 24:1183–1190
35. Wuensch BJ, Eberman KW (2000) Order-disorder phenomena in $A_2B_2O_7$ pyrochlore oxides. J Metals 52:19–21
36. Werner PE, Erikson L, Westdahl M (1985) *TREOR*, a semi-exhaustive trial-and-error powder indexing program for all symmetries. J Appl Cryst 18:367–370
37. de Wolff PM (1968) A simplified criterion for the reliability of a powder pattern indexing. J Appl Cryst 1:108–113

Journal : Large 10853 | Dispatch : 5-6-2014 | Pages : 10
Article No. : 8361 | ☐ LE | ☐ TYPESET
MS Code : JMSC-D-14-00482 | ☑ CP | ☑ DISK